Editors' Suggestion

Microscopic details of two-dimensional spectroscopy of one-dimensional quantum Ising magnets

GiBaik Sim,[1,2] Frank Pollmann,[1,2] and Johannes Knolle[1,2,3]

[1]*Physics Department, TUM School of Natural Sciences, Technical University of Munich, 85748 Garching, Germany*
[2]*Munich Center for Quantum Science and Technology (MCQST), Schellingstr. 4, 80799 München, Germany*
[3]*Blackett Laboratory, Imperial College London, London SW7 2AZ, United Kingdom*

(Received 9 May 2023; accepted 4 October 2023; published 17 October 2023)

The identification of microscopic systems describing the low-energy properties of correlated materials has been a central goal of spectroscopic measurements. We demonstrate how two-dimensional (2D) nonlinear spectroscopy can be used to distinguish effective spin systems whose linear responses show similar behavior. Motivated by recent experiments on the quasi-1D Ising magnet $CoNb_2O_6$, we focus on two proposed systems—the ferromagnetic twisted Kitaev spin chain with bond dependent interactions and the transverse field Ising chain. The dynamical spin structure factor probed in linear response displays similar broad spectra for both systems from their fermionic domain wall excitations. In sharp contrast, the 2D nonlinear spectra of the two systems show clear qualitative differences: those of the twisted Kitaev spin chain contain off-diagonal peaks originating from the bond dependent interactions and transitions between different fermion bands absent in the transverse field Ising chain. We discuss the different signatures of spin fractionalization in integrable and nonintegrable regimes of the systems and their connection to experiments.

DOI: 10.1103/PhysRevB.108.134423

I. INTRODUCTION

The possibility to understand the microscopics of correlated quantum materials is closely connected to advances in spectroscopic techniques [1]. In addition to the traditional use of linear response probes, *two-dimensional coherent spectroscopy* (2DCS) [2,3] promises to provide additional information because of its ability to access multitime correlation functions sensitive to interactions between excitations. Probing the nonlinear optical response of the target system, 2DCS has been used to study vibrational and electronic excitations in molecules [4] and exciton resonances in quantum wells [5,6]. Additionally, recent advances with terahertz sources put the technique in the proper energy ranges for studying optical excitations of magnetic materials [7]. Unlike conventional one-dimensional (1D) spectroscopy and standard inelastic neutron scattering, 2DCS reveals not only the linear response of spin flips but has more direct access to the interplay of intrinsic excitations of magnets. Along this line, it was theoretically proposed that such interplay can be used to identify the presence of fractionalized particles [8–12], their self-energies [13], and the effect of interactions between them [14,15].

In this paper, we show that 2DCS can be a powerful tool for quantifying the microscopic parameters of quantum magnets. Concretely, we consider 2DCS as a means for distinguishing between two alternative descriptions of Ising chain magnets—the ferromagnetic twisted Kitaev spin chain (TKSC) with bond dependent spin exchange terms and the transverse field Ising chain (TFIC). In both cases, spin flip excitations fractionalize into domain wall excitations leading to similar linear response spectra but distinct qualitative differences in 2DCS.

Our study is motivated by previous works [16,17], which proposed that the field dependent behavior of $CoNb_2O_6$, long believed the best example of an Ising chain magnet [18–25], is in fact well captured by the TKSC. We first confirm that the linear response of the TKSC and TFIC is indeed similar, which complicates the identification of the microscopic description. Second, as our main result, we establish that there are significant differences between the 2D spectra of the TKSC and TFIC: (i) the magnetic second order susceptibility $\chi^{(2)}_{xxx}$ vanishes for the TKSC due to the presence of a $\hat{z}$-glide symmetry [16] while it is finite for the TFIC; (ii) the third order susceptibility $\chi^{(3)}_{xxxx}$ contains off-diagonal peaks from interband fermion transitions for the TKSC which are absent for the TFIC. Taking into account the experimentally relevant canting angle [26] between the crystal axis $\hat{a}$ and local axis $\hat{x}$ in $CoNb_2O_6$, we also compute the easier accessible 2D spectrum, $\chi^{(2)}_{yyy}$, of the TKSC. We find that $\chi^{(2)}_{yyy}$ becomes finite and contains off-diagonal signals with an external transverse field along $\hat{y}$, which breaks the $\hat{z}$-glide symmetry and the integrability of the system, using infinite matrix-product state (MPS) techniques [27–29]. We also confirm that such peaks persist in the presence of additional XX-type interactions, which can be relevant in $CoNb_2O_6$ [16,30,31].

Our paper is structured as follows. We first briefly review the TKSC and TFIC in Sec. II and confirm the similarity of their linear response spectra in Sec. III. We then discuss their nonlinear response and compare the differences of the 2DCS spectra in Sec. IV. In Sec. V, we investigate the effect of glide symmetry breaking on the 2DCS spectra of the TKSC and discuss the relevance of our findings for $CoNb_2O_6$. We conclude with a discussion and outlook in Sec. VI.

II. TWO ISING MAGNETS

We first introduce the TKSC [17] described by the following Hamiltonian:

$$H_{\mathrm{TKSC}} = -J\sum_{i=1}^{L'}[\tilde{\sigma}_{2i-1}(\theta)\tilde{\sigma}_{2i}(\theta) + \tilde{\sigma}_{2i}(-\theta)\tilde{\sigma}_{2i+1}(-\theta)]. \quad (1)$$

Here, $J > 0$ is the ferromagnetic exchange parameter, $L' = L/2$ is the number of unit cells, each containing two sites, and $\tilde{\sigma}_i(\theta) \equiv \cos(\theta)\sigma_i^z + \sin(\theta)\sigma_i^y$. Such linear combinations imply that the interaction on each odd (even) bond is characterized by the Ising easy axis with an angle $\pm\theta$ [32]. The TKSC respects two different glide symmetries, $G_y \equiv T_c e^{(i\pi/2)\sum_i^L \sigma_i^y}$ and $G_z \equiv T_c e^{(i\pi/2)\sum_i^L \sigma_i^z}$, where T_c is a translation operator by half a unit cell [16]. When $0 \leqslant \theta < \pi/4$, the TKSC admits a doubly degenerate ferromagnetic ground state, polarized along the easy axis $\hat{z}$. In this regime, the ground state spontaneously breaks G_y, but still preserves one global symmetry G_z. Below we fix $\theta = \pi/12$ for the TKSC which is close to the value used in Ref. [17] to describe $CoNb_2O_6$. In this case, the elementary excitations of the TKSC are domain walls between the two degenerate ground states, similar to the ferromagnetic TFIC with interactions given by

$$H_{\text{TFIC}} = -J\sum_{i=1}^{L}\sigma_i^z\sigma_{i+1}^z - h_x\sum_{i=1}^{L}\sigma_i^x. \tag{2}$$

Below, we fix $h_x/J = 1/2$ at which the system also stabilizes a doubly degenerate ferromagnetic ground state.

Performing the Jordan-Wigner transformation, which maps the Pauli operators to fermion operators, and Bogoliubov transformation, we can rewrite both the TKSC and TFIC as noninteracting fermionic systems. The TKSC then reads

$$H_{\text{TKSC}} = \sum_{k>0} l_k(\alpha_k^\dagger\alpha_k - \alpha_{-k}\alpha_{-k}^\dagger) + \lambda_k(\beta_k^\dagger\beta_k - \beta_{-k}\beta_{-k}^\dagger). \tag{3}$$

Here, α_k and β_k represent the two different bands with dispersion relations $2l_k$ and $2\lambda_k$ respectively for the TKSC in momentum space representation (see Appendix A for details). The Hamiltonian in Eq. (3) can be interpreted as a four level system with a momentum pair $\pm k$, where energies of states are $-\lambda_k$, $-l_k$, l_k, and λ_k. In the following, we denote such states by $|0\rangle$, $|1\rangle$, $|2\rangle$, and $|3\rangle$. Thus the TKSC corresponds to an ensemble of decoupled four level systems. The TFIC in fermionic formulation reads

$$H_{\text{TFIC}} = \sum_{k>0}\epsilon_k(\gamma_k^\dagger\gamma_k - \gamma_{-k}\gamma_{-k}^\dagger), \tag{4}$$

where γ_k represents a single band with dispersion $2\epsilon_k$. The TFIC corresponds to an ensemble of decoupled two level systems with the energy gap $2\epsilon_k$ and is clearly distinct from the TKSC.

III. LINEAR RESPONSE STRUCTURE FACTOR

We first briefly compare the linear response, i.e., the dynamical structure factor

$$S_{xx}(k,\omega) = \frac{1}{4}\int dt \sum_j e^{i\omega t - ik(r_j - r_{L/2})}\langle\sigma_j^x(t)\sigma_j^x(0)\rangle \tag{5}$$

of the TKSC and TFIC [33,34]. In both systems, a spin flip excites a pair of domain walls (fermions) with net momentum k. Such fractionalization of the excitations only yields a broad continuous spectrum. In Fig. 1, we plot $S_{xx}(k,\omega)$ computed using MPS simulations with open boundary conditions (see Appendix B for details) [35]. The two systems show a qualitatively similar spectrum, indicating the difficulty of using a conventional probe like inelastic neutron scattering for distinguishing between the two system descriptions.[1]

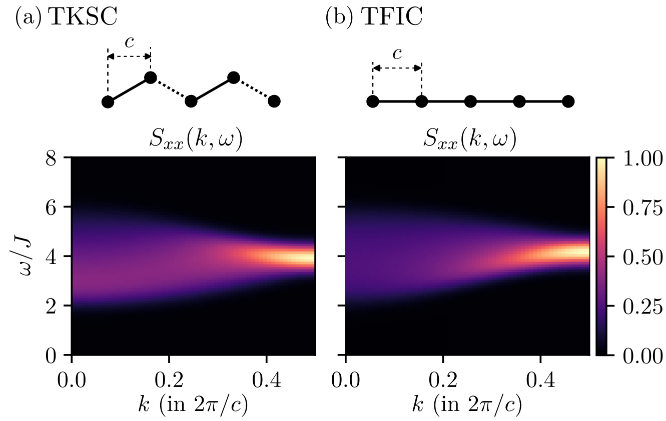

FIG. 1. (a), (b) Dynamical spin structure factor $S_{xx}(k,\omega)$ of the ferromagnetic TKSC and TFIC. k and ω represent the momentum and frequency, respectively. The MPS simulations are done for an open chain using the time evolving block decimation method [37,38], which provides an efficient way to perform a real time evolution in 1D spin systems.

IV. NONLINEAR RESPONSE

Next, we introduce the two-pulse experiment and show how it can detect the nonlinear magnetic susceptibilities of target systems. We closely follow Ref. [7] and Ref. [8].

In this setup, two magnetic pulses B_0 and B_τ both polarized along $\hat{\alpha}$ direction,

$$B(T) = B_0\delta(T)\hat{\alpha} + B_\tau\delta(T-\tau)\hat{\alpha}, \tag{6}$$

arrive at the target system at times $T = 0$ and $T = \tau$. Here, the magnetic field is assumed to be spatially homogeneous. The two pulses induce a magnetization $M_{0,\tau}^\alpha(T)$ of the system measured at time $T = \tau + t$. To remove the induced magnetization from the linear response, two additional experiments each with a single pulse B_0 or B_τ are performed which measure $M_0^\alpha(T)$ or $M_\tau^\alpha(T)$, respectively. The nonlinear magnetization $M_{NL}^\alpha(T) \equiv M_{0,\tau}^\alpha(T) - M_0^\alpha(T) - M_\tau^\alpha(T)$ can then be expanded as

$$\begin{aligned} M_{NL}^\alpha(T) = {} & B_0 B_\tau \chi_{\alpha\alpha\alpha}^{(2)}(t,\tau+t) \\ & + (B_0)^2 B_\tau \chi_{\alpha\alpha\alpha\alpha}^{(3,1)}(t,\tau+t,\tau+t) \\ & + B_0(B_\tau)^2\chi_{\alpha\alpha\alpha\alpha}^{(3,2)}(t,t,\tau+t) + O(B^4), \end{aligned} \tag{7}$$

which directly gives the second and higher order magnetic susceptibilities.

[1] We note that similarity can be understood by the fact that staggered terms induce hopping of domain walls in TKSC similar to the transverse field term in TFIC [36].

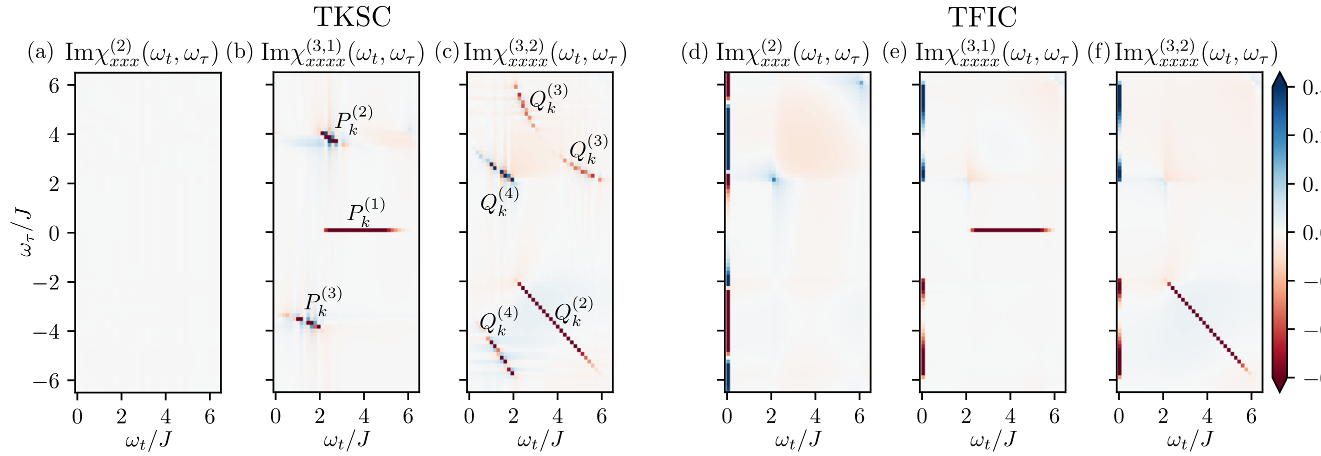

FIG. 2. (a)–(c) From left to right: imaginary part of Fourier transformed $\chi^{(2)}_{xxx}(t,\tau+t)$, $\chi^{(3,1)}_{xxxx}(t,\tau+t,\tau+t)$, and $\chi^{(3,2)}_{xxxx}(t,t,\tau+t)$ of the TKSC. (d)–(f) From left to right: $\mathrm{Im}\,\chi^{(2)}_{xxx}(\omega_t,\omega_\tau)$, $\mathrm{Im}\,\chi^{(3,1)}_{xxxx}(\omega_t,\omega_\tau)$, and $\mathrm{Im}\,\chi^{(3,2)}_{xxxx}(\omega_t,\omega_\tau)$ of the TFIC. The 2D spectra are obtained for a periodic chain of size $L=220$ over the time range $Jt, J\tau=40$. Since $\mathrm{Im}\,\chi^{(n)}(\omega_t,\omega_\tau)=-\mathrm{Im}\,\chi^{(n)}(-\omega_t,-\omega_\tau)$, the results are only shown in the first and fourth frequency quadrant. See Appendix C for the real part. All the data are rescaled such that the maximal absolute value is 1.

Due to its exact solubility, we can analytically calculate the $\chi^{(2)}_{xxx}$ and $\chi^{(3)}_{xxxx}$ susceptibilities of the TKSC (see Appendix C for details). A formulation for the TFIC is explicitly given in Ref. [8].

A. Second order susceptibility

We start with the second order susceptibility, which is given by

$$\chi^{(2)}_{xxx}(t,\tau+t)=\frac{-\Theta(t)\Theta(\tau)}{L}\langle[[M^x(\tau+t),M^x(\tau)],M^x(0)]\rangle, \tag{8}$$

where $M^x(T)\equiv\frac{1}{2}\sum_i e^{iHT}\sigma_i^x e^{-iHT}$ represents the total magnetization along $\hat{x}$ direction in the Heisenberg picture [8]. To formulate $\chi^{(2)}_{xxx}$ of the TKSC, one needs to calculate expectation values of the form

$$\langle g|M^x(T_1)M^x(T_2)M^x(T_3)|g\rangle. \tag{9}$$

Here, $|g\rangle$ represents the ferromagnetic ground state of the TKSC, which is invariant under the $\hat{z}$-glide operation: $G_z|g\rangle=|g\rangle$. At the same time, the operator $M^x(T_1)M^x(T_2)M^x(T_3)$ is odd under the same glide operation: $G_zM^x(T_1)M^x(T_2)M^x(T_3)G_z^\dagger=-M^x(T_1)M^x(T_2)M^x(T_3)$. The invariance of $|g\rangle$ and oddness of the operator $M^x(T_1)M^x(T_2)M^x(T_3)$ under G_z makes Eq. (9) vanish and $\chi^{(2)}_{xxx}$ is zero [Fig. 2(a)] unless additional symmetry-breaking terms are added to the system. Such a nonlinear spectrum of the TKSC is clearly distinct from the one of the TFIC [Fig. 2(d)] which contains a strong terahertz rectification signal in $\chi^{(2)}_{xxx}$ [8]. When the second order susceptibility vanishes, the third or higher order susceptibilities dominate the nonlinear response of the system.

B. Third order susceptibility

We now turn to the next leading order response, i.e., $\chi^{(3,1)}_{xxxx}$ and $\chi^{(3,2)}_{xxxx}$. Using the basis introduced in Eq. (3), we can also express $M^x(T)$ in terms of fermion operators and obtain the formula for the third order susceptibility of the TKSC analytically:

$$\chi^{(3,1)}_{xxxx}(t,\tau+t,\tau+t)=\frac{\Theta(t)\Theta(\tau)}{L}\sum_{k>0}P_k^{(1)}+P_k^{(2)}+P_k^{(3)},$$

with

$$P_k^{(1)}=-8c_k^4[\sin(2l_kt)+(l_k\leftrightarrow\lambda_k)],$$
$$P_k^{(2)}=8\left(c_k^4-c_k^2\right)[\sin(2l_kt+(l_k+\lambda_k)\tau)+(l_k\leftrightarrow\lambda_k)],$$
$$P_k^{(3)}=8\left(c_k^2-c_k^4\right)[\sin((l_k-\lambda_k)t+(l_k+\lambda_k)\tau)+(l_k\leftrightarrow\lambda_k)],$$

where c_k is the matrix element of the magnetization along $\hat{x}$ direction in the basis introduced in Eq. (3) (see Appendix C for definitions). In $\chi^{(3,1)}_{xxxx}$, $P_k^{(1-3)}$ represent different two-time evolution paths of a fermion pair with momenta $\pm k$ excited by the pulses. Employing the four level picture of the fermionic Hamiltonian in momentum space, we can interpret $P_k^{(1)}$ as follows. The second pulse in the two-pulse setup induces transitions between $|1\rangle$ and $|2\rangle$, resulting in an oscillatory signal with frequency $2l_k$ throughout the time interval t between the second pulse and measurement. This signal is encoded in the first term of $P_k^{(1)}$. The term is not oscillatory in τ and gives rise to a peak at $(\omega_t,\omega_\tau)=(2l_k,0)$ in the frequency domain [Fig. 2(b)]. Interpreting ω_t as the detecting frequency and ω_τ as the pumping frequency, the signal can be understood as a pump probe signal. Such a signal is also contained in $\chi^{(3,1)}_{xxxx}$ of the TFIC [Fig. 2(e)]. $P_k^{(2)}$ contains terms which are oscillatory both in t and τ. Such terms produce non-rephasing-like signals at $(\omega_t,\omega_\tau)=(2l_k,l_k+\lambda_k)$ and $(\omega_t,\omega_\tau)=(2\lambda_k,l_k+\lambda_k)$, giving rise to off-diagonal peaks in the first frequency quadrant as shown in Fig. 2(b). $P_k^{(3)}$ is distinct from $P_k^{(1,2)}$ in that it contains a term where t and τ come with opposite signs: the dephasing process during τ is followed by the rephasing process during t. This process induces rephasing like signals which appear as off-diagonal peaks in the fourth quadrant, mirroring the energy range of corresponding fermion pairs [Fig. 2(b)].

Qualitatively different signals are encoded in $\chi^{(3,2)}_{xxxx}$, which is given as

$$\chi^{(3,2)}_{xxxx}(t,t,\tau+t)=\frac{\Theta(t)\Theta(\tau)}{L}\sum_{k>0}Q^{(1)}_k+Q^{(2)}_k+Q^{(3)}_k+Q^{(4)}_k,$$

with

$$\begin{aligned}
Q^{(1)}_k&=-4c_k^2[\sin(2l_k(t+\tau))+(l_k\leftrightarrow\lambda_k)],\\
Q^{(2)}_k&=-4c_k^4[\sin(2l_k(t-\tau))+(l_k\leftrightarrow\lambda_k)],\\
Q^{(3)}_k&=4\big(c_k^4-c_k^2\big)[\sin(2\lambda_k t+2l_k\tau)+(l_k\leftrightarrow\lambda_k)],\\
Q^{(4)}_k&=8\big(c_k^2-c_k^4\big)[\sin((\lambda_k-l_k)t+2l_k\tau)+(l_k\leftrightarrow\lambda_k)].
\end{aligned}$$

The presence of $Q^{(1)}_k$ and $Q^{(2)}_k$ results in the appearance of diagonal peaks in the frequency domain [Fig. 2(c)]. $Q^{(1)}_k$ is oscillatory in $t+\tau$ and induces diffusive nonrephasing signals in the first quadrant. The signals are barely visible since the amplitude is relatively small for $\theta=\pi/12$. $Q^{(2)}_k$ is unique in that t and τ come with opposite signs but with the same oscillation frequency $2l_k$ or $2\lambda_k$. Unlike other terms, the phase accumulated during τ is perfectly canceled out during t, regardless of the oscillation frequency. This corresponds to the "spinon echo," which was discovered in Ref. [8] for the TFIC [Fig. 2(f)] and results in a diagonal rephasing signal in the fourth quadrant [Fig. 2(c)]. $Q^{(3)}_k$ produces non-rephasing-like signals at $(\omega_t,\omega_\tau)=(2\lambda_k,2l_k)$ and $(\omega_t,\omega_\tau)=(2l_k,2\lambda_k)$, giving rise to off-diagonal peaks in the first quadrant [Fig. 2(c)]. $Q^{(4)}_k$ contains terms that induce strong off-diagonal peaks in the frequency domain, reflecting the energy range of corresponding states [Fig. 2(c)].

C. Discussion of second and third order susceptibilities

The 2D spectra of the TKSC and the TFIC show qualitative differences. First, $\chi^{(2)}_{xxx}$ of the TKSC vanishes due to $\hat{z}$-glide symmetry, while it is finite for the TFIC. In such a situation, $\chi^{(3)}_{xxxx}$ dominates the nonlinear response of the system. $\chi^{(3)}_{xxxx}$ of the TKSC contains off-diagonal peaks coming from the staggered interactions, in sharp contrast to $\chi^{(3)}_{xxxx}$ of the TFIC. The emergence of such off-diagonal peaks can be used to distinguish the TKSC from the TFIC.

V. GLIDE SYMMETRY AND $CoNb_2O_6$

A. Integrable cases

We now add a transverse field term $-h_x\sum_i^L\sigma_i^x$ to the TKSC in Eq. (1), which breaks the $\hat{z}$-glide symmetry and makes the leading nonlinear susceptibility $\chi^{(2)}_{xxx}$ finite. We then investigate whether off-diagonal peaks arise in $\chi^{(2)}_{xxx}(\omega_t,\omega_\tau)$, revealing the staggered interactions. Note, we only focus on the regime where the ground state remains ferromagnetic. The transverse field term is also quadratic in fermionic operators, allowing for an analytic calculation of nonlinear susceptibilities (see Appendix D for details). In Fig. 3(a), we plot $\mathrm{Im}\chi^{(2)}_{xxx}(\omega_t,\omega_\tau)$ at a low transverse field $h_x/J=1/20$. First, it contains a dominant vertical terahertz rectification signal similar to the one of the TFIC [8]. At the same time, off-diagonal

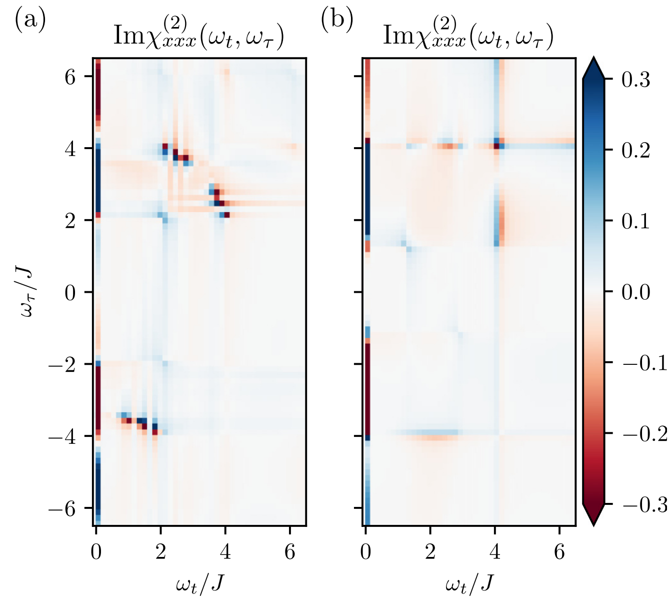

FIG. 3. $\mathrm{Im}\chi^{(2)}_{xxx}(\omega_t,\omega_\tau)$ of the TKSC with (a) a small transverse field $h_x/J=1/20$ and (b) a strong transverse field $h_x/J=1/2$. The calculations are done for a periodic chain of $L=220$ and over the time range $Jt, J\tau=40$.

peaks appear, reflecting the energy range of corresponding fermion pairs. In the strong field regime $h_x/J=1/2$, the amplitude of the off-diagonal peaks becomes relatively weak as shown in Fig. 3(b). It can be understood by the fact that the strength of the staggered terms in the TKSC, given by $\pm YZ$-type interactions in Eq. (1), becomes relatively small in the strong field limit $h_x/J\rightarrow 1$ where the full system behaves like the TFIC.

B. Nonintegrable cases and $CoNb_2O_6$

Our results can be compared to the quasi-1D Ising magnet $CoNb_2O_6$, which was recently proposed as a close material realization of the TKSC [16,17]. In $CoNb_2O_6$, cobalt atoms are surrounded by distorted octahedra formed by oxygen atoms. These edge-sharing octahedra form an isolated zigzag 1D chain along the crystal axis $\hat{c}$, as shown in Fig. 4(a). In this material, the local axis $\hat{y}$ is exactly aligned to the crystal axis $\hat{b}$, unlike the local axis $\hat{x}$, which makes an angle $\phi=\pm31^\circ$ with the crystal axis $\hat{a}$ [17,26]. In this case, $\chi^{(2)}_{yyy}=\chi^{(2)}_{bbb}$ would be experimentally more pronounced than $\chi^{(2)}_{xxx}$, which is distinct from $\chi^{(2)}_{aaa}$. On the other hand, the accurate description of $CoNb_2O_6$ may comprise subdominant XX-type interactions, which are allowed by the crystal symmetry, as revealed by neutron scattering experiments [16,30,31]. In this regard, we focus on the system given as

$$\begin{aligned}
H=&-J\sum_{i=1}^{L'}[\tilde{\sigma}_{2i-1}(\theta)\tilde{\sigma}_{2i}(\theta)+\tilde{\sigma}_{2i}(-\theta)\tilde{\sigma}_{2i+1}(-\theta)]\\
&-J_x\sum_i^L\sigma_i^x\sigma_{i+1}^x-h_y\sum_i^L\sigma_i^y,
\end{aligned}\tag{10}$$

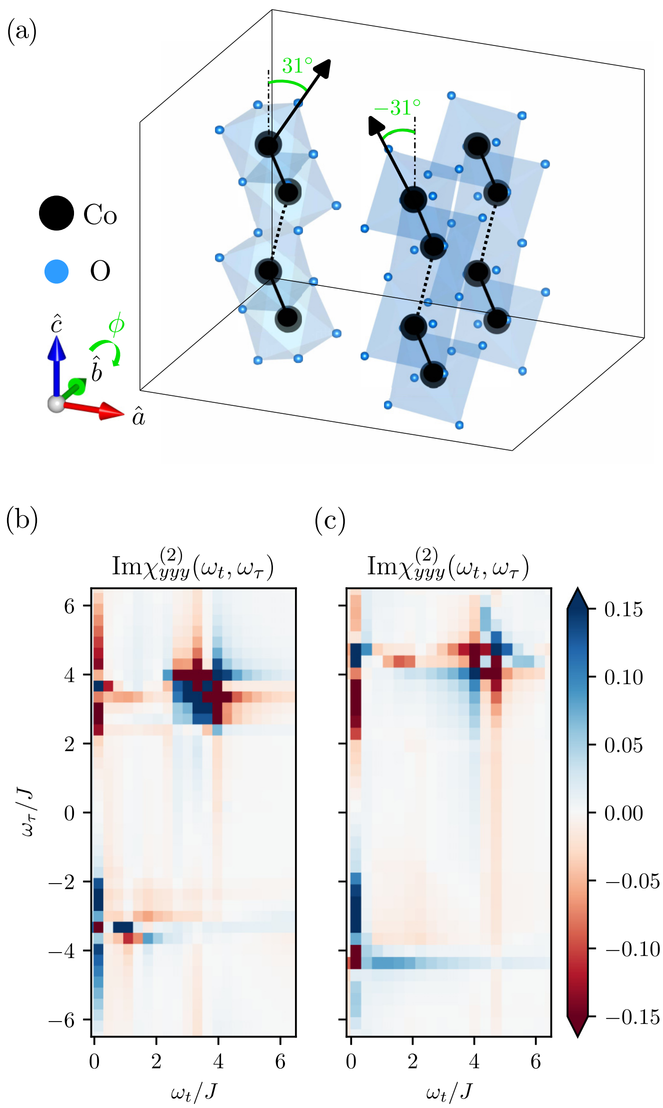

FIG. 4. (a) Unit cell of $CoNb_2O_6$ where each zigzag chain is aligned along the crystal axis $\hat{c}$. The black arrows indicate the two different local $\hat{z}$ axes, which lie in the $\hat{a}-\hat{c}$ plane with the tilting angle $\phi=\pm31^\circ$ [17,26]. (b) $\mathrm{Im}\chi^{(2)}_{yyy}(\omega_t,\omega_\tau)$ with $\theta=\pi/12$, $J_x/J=0$, and $h_y/J=1/20$. (c) $\mathrm{Im}\chi^{(2)}_{yyy}(\omega_t,\omega_\tau)$ with $\theta=\pi/12$, $J_x/J=1/10$, and $h_y/J=1/20$.

which contains the additional XX-type interaction and transverse field term along the $\hat{y}$ axis. Since the $\hat{b}$ and $\hat{y}$ axes are aligned, the transverse term can be included by simply applying an external field along the crystal axis $\hat{b}$ to $CoNb_2O_6$. The system is nonintegrable, except in two cases with $\theta=0$ or $\theta\neq0$, $J_x=0$, and $h_y=0$.

We now calculate $\chi^{(2)}_{yyy}$ of the system in the ferromagnetic regime with fixed $\theta=\pi/12$, which is close to the value given in Ref. [17] for $CoNb_2O_6$, using infinite MPS techniques [29]. The techniques provide a way to calculate the numerically exact $\chi^{(2)}_{yyy}$ for the nonintegrable cases and the calculations are done with window size $L=120$ and over the time range $Jt, J\tau=20$. We checked the dependence of $\chi^{(2)}_{yyy}$ on the bond dimension χ and the time step δt, settling on $\chi_{\max}=1000$ and $\delta t=0.01/J$. We first notice that $\chi^{(2)}_{yyy}$ vanishes unless the $\hat{z}$-glide symmetry breaking term is finite, $h_y\neq0$. In Fig. 4(b), we plot $\mathrm{Im}\chi^{(2)}_{yyy}(\omega_t,\omega_\tau)$ of the system with $J_x/J=0$ and $h_y/J=1/20$. Analogous to $\mathrm{Im}\chi^{(2)}_{xxx}(\omega_t,\omega_\tau)$ of the TKSC with the transverse field along the $\hat{x}$ direction, it also contains off-diagonal peaks which can signal the presence of the staggered interactions. We also investigate the effect of additional XX-type interactions on such off-diagonal peaks regarding $CoNb_2O_6$. As shown in Fig. 4(c) for the system with $J_x/J=1/10$ and $h_y/J=1/20$, such peaks still appear though the amplitude becomes relatively weak.

VI. CONCLUSIONS

In the present work, we propose a way to distinguish two similar systems, i.e., the ferromagnetic TKSC and TFIC, using 2DCS. In both systems, elementary spin flips fractionalize into domain wall excitations, resulting in a qualitatively similar continuum in the linear response dynamical structure factor. In contrast, we show that the 2D nonlinear spectrum as a function of ω_τ and ω_t, associated with the time interval between a probe and measurement pulse, offers a clear way to discern the two systems. Unlike the TFIC, the second order susceptibility $\chi^{(2)}_{xxx}$ vanishes for the TKSC due to the presence of a $\hat{z}$-glide symmetry. Moreover, the third order susceptibility $\chi^{(3)}_{xxxx}$ of the TKSC contains non-rephasing- and rephasing-like signals which appear as off-diagonal peaks in the frequency domain, originating from the presence of bond dependent interactions.

Regarding the canted structure of $CoNb_2O_6$, a possible material realization of the TKSC, we also investigate the second order susceptibility $\chi^{(2)}_{yyy}$. For the nonintegrable regime we have employed the infinite MPS method for calculating the nonlinear response. First, we find that $\chi^{(2)}_{yyy}$ of the TKSC vanishes unless additional $\hat{z}$-glide symmetry breaking terms are included. Second, we observe the emergence of off-diagonal peaks with an external transverse field along the $\hat{y}$ axis. Such peaks persist with additional XX-type interactions, which can be subdominant in $CoNb_2O_6$. We expect our results will shed light on the unambiguous identification of the correct microscopic description of $CoNb_2O_6$.

Advances in spectroscopic methods, accessible frequency ranges, and improved energy resolution allow for a more precise understanding of correlated quantum systems. We expect 2DCS to be an excellent tool for determining the microscopic parameters of quantum magnets, not only for the one-dimensional example considered here but also for two- and three-dimensional frustrated magnets.

Data analysis and simulation codes are available on Zenodo upon reasonable request [39].

ACKNOWLEDGMENTS

We thank R. Coldea, N. P. Armitage, M. Drescher, H.-K. Jin, W. Choi, N. Perkins, S. Gopalakrishnan, and Z. Wang for insightful discussions related to this work. G.B.S. thanks P. d'Ornellas for detailed comments on the manuscript. G.B.S. is funded by the European Research Council (ERC) under the European Unions Horizon 2020 research and innovation program (Grant Agreement No. 771537). F.P. acknowledges the support of the Deutsche Forschungsgemeinschaft (DFG, German Research Foundation) under Germany's Excellence Strategy EXC-2111-390814868. J.K. acknowledges support from the Imperial-TUM flagship partnership. The research is part of the Munich Quantum Valley, which is supported by the Bavarian state government with funds from the Hightech Agenda Bayern Plus. Tensor network calculations were performed using the TeNPy Library [40].

APPENDIX A: JORDAN-WIGNER FORMALISM

In this Appendix, we introduce the Jordan-Wigner formulation of the TKSC. The TKSC is written as

$$H_{\text{TKSC}} = -J\sum_{i=1}^{L'}(\tilde{\sigma}_{2i-1}(\theta)\tilde{\sigma}_{2i}(\theta) + \tilde{\sigma}_{2i}(-\theta)\tilde{\sigma}_{2i+1}(-\theta)).$$

We now introduce the Jordan-Wigner transformation, which maps the Pauli operators to fermionic operators through the relations [32]

$$\begin{aligned}\sigma_j^x &= 1 - 2c_j^\dagger c_j,\\ \sigma_j^y &= -i(c_j^\dagger - c_j)\prod_{i<j}(1-2c_i^\dagger c_i),\\ \sigma_j^z &= (c_j^\dagger + c_j)\prod_{i<j}(1-2c_i^\dagger c_i).\end{aligned} \tag{A1}$$

Using Eq. (A1), we arrive at a bilinear form in terms of spinless fermions:

$$\begin{aligned}H_{\text{TKSC}} = -J\sum_{i=1}^{L'}[&e^{-2i\theta}c_{2i-1}^\dagger c_{2i}^\dagger + c_{2i-1}^\dagger c_{2i}\\ &+ e^{+2i\theta}c_{2i}^\dagger c_{2i+1}^\dagger + c_{2i}^\dagger c_{2i+1} + \text{H.c.}].\end{aligned} \tag{A2}$$

We then adopt the Fourier transformation $c_{2j-1} = \frac{1}{\sqrt{L'}}\sum_k e^{-ikj}a_k$, $c_{2j} = \frac{1}{\sqrt{L'}}\sum_k e^{-ikj}b_k$ with the discrete momenta $k = \frac{n\pi}{L'}$, $n = -(L'-1), \ldots, (L'-3), (L'-1)$. The TKSC now takes the form

$$H_{\text{TKSC}} = -J\sum_k[B_k a_k^\dagger b_{-k}^\dagger + A_k a_k^\dagger b_k - A_k^* a_k b_k^\dagger - B_k^* a_k b_{-k}], \tag{A3}$$

where $A_k = 1 + e^{ik}$ and $B_k = e^{-2i\theta} - e^{i(k+2\theta)}$. To diagonalize the Hamiltonian Eq. (A3), we write it in a matrix form as

$$H_{\text{TKSC}} = \sum_{k>0}(a_k^\dagger, a_{-k}, b_k^\dagger, b_{-k})\hat{M}_k\begin{pmatrix}a_k\\ a_{-k}^\dagger\\ b_k\\ b_{-k}^\dagger\end{pmatrix}, \tag{A4}$$

where

$$\hat{M}_k = \begin{pmatrix}0 & 0 & S_k & P_k+Q_k\\ 0 & 0 & P_k-Q_k & -S_k\\ S_k^* & P_k^*-Q_k^* & 0 & 0\\ P_k^*+Q_k^* & -S_k^* & 0 & 0\end{pmatrix},$$

with $P_k = iJ(1+e^{ik})\sin 2\theta$, $Q_k = -J(1-e^{ik})\cos 2\theta$, and $S_k = -J(1+e^{ik})$. The diagonalization of Eq. (A4) is achieved by the Bogoliubov transformation

$$(\alpha_k^\dagger, \alpha_{-k}, \beta_k^\dagger, \beta_{-k})\,\hat{U}_k = (a_k^\dagger, a_{-k}, b_k^\dagger, b_{-k}). \tag{A5}$$

The Hamiltonian is now diagonalized in the new basis as

$$H_{\text{TKSC}} = \sum_{k>0}\left[l_k(\alpha_k^\dagger\alpha_k - \alpha_{-k}\alpha_{-k}^\dagger) + \lambda_k(\beta_k^\dagger\beta_k - \beta_{-k}\beta_{-k}^\dagger)\right], \tag{A6}$$

where $l_k = \sqrt{\xi_k - \sqrt{\xi_k^2 - \tau_k^2}}$, $\lambda_k = \sqrt{\xi_k + \sqrt{\xi_k^2 - \tau_k^2}}$ with $\xi_k = |P_k|^2 + |Q_k|^2 + |S_k|^2$, and $\tau_k = |P_k^2 - Q_k^2 + S_k^2|$.

APPENDIX B: DETAILS OF MPS SIMULATION FOR THE DYNAMICAL STRUCTURE FACTOR

In this Appendix, we provide details of the MPS simulations for the dynamical structure factor [35]

$$\begin{aligned}S_{xx}(k,\omega) &= \frac{1}{4}\int dt\sum_j e^{i\omega t - ik(r_j - r_{L/2})}\langle\sigma_j^x(t)\sigma_{L/2}^x(0)\rangle\\ &= \frac{1}{4}\int dt\sum_j\left[e^{i\omega t - ik(r_j - r_{L/2})}e^{iE_g t}\langle g|\sigma_j^x e^{-iHt}\sigma_{L/2}^x|g\rangle G(t)\right].\end{aligned}$$

(1) Find an MPS approximation of the ground state $|g\rangle$ with an energy E_g using the density matrix renormalization group.

(2) Apply a local operator $\sigma_{L/2}^x$ and obtain $\sigma_{L/2}^x|g\rangle$.

(3) Perform a real time evolution following the local quench $\sigma_{L/2}^x$ using the time evolving block decimation method [37,41] to get an MPS which represents $e^{-iHt}\sigma_{L/2}^x|g\rangle$.

(4) Evaluate an overlap of two MPS "bra" and "ket" to obtain $\langle g|\sigma_j^x e^{-iHt}\sigma_{L/2}^x|g\rangle$.

(5) Multiply $e^{iE_g t}$ and $\langle g|\sigma_j^x e^{-iHt}\sigma_{L/2}^x|g\rangle$.

(6) Apply a discrete Fourier transformation in space that yields the momentum-resolved time-dependent data $S_{xx}(k,t)$.

(7) Perform a Fourier transformation of the time series convoluted with a Gaussian window function $G(t) = e^{-t^2/2\sigma^2}$ to prevent Gibbs oscillations [16,42,43].

For the result given in Fig. 1, we set the system size $L = 120$, time step size $\delta t = 0.02J$, total simulation time $t_{\max} = 60J$, maximum bond dimension $\chi_{\max} = 500$, and the Gaussian envelope parameter $\sigma = 0.05$.

APPENDIX C: MAGNETIC SUSCEPTIBILITIES OF THE TKSC

Here, we analytically formulate the linear and nonlinear magnetic susceptibilities of the TKSC. M^x, the total magnetization of the target system along $\hat{x}$ direction, in fermionic formulation reads

$$\begin{aligned} M^x &= \frac{1}{2}\sum_i^{L'}\left(\sigma^x_{2i-1}+\sigma^x_{2i}\right)=\sum_{k>0} m^x_k \\ &= \sum_{k>0}[-a_k^\dagger a_k + a_{-k}a^\dagger_{-k} - b^\dagger_k b_k + b_{-k}b^\dagger_{-k}]. \end{aligned} \tag{C1}$$

M^x can be rewritten in the basis introduced in Eq. (A5):

$$\begin{aligned} M^x &= \sum_{k>0}[-a_k^\dagger a_k + a_{-k}a^\dagger_{-k} - b^\dagger_k b_k + b_{-k}b^\dagger_{-k}] = (a_k^\dagger, a_{-k}, b_k^\dagger, b_{-k})\begin{pmatrix}-1&0&0&0\\0&1&0&0\\0&0&-1&0\\0&0&0&1\end{pmatrix}\begin{pmatrix}a_k\\a^\dagger_{-k}\\b_k\\b^\dagger_{-k}\end{pmatrix} \\ &= (\alpha_k^\dagger, \alpha_{-k}, \beta_k^\dagger, \beta_{-k})\hat{U}_k\begin{pmatrix}-1&0&0&0\\0&1&0&0\\0&0&-1&0\\0&0&0&1\end{pmatrix}\hat{U}_k^\dagger\begin{pmatrix}\alpha_k\\\alpha^\dagger_{-k}\\\beta_k\\\beta^\dagger_{-k}\end{pmatrix} \\ &= (\alpha_k^\dagger, \alpha_{-k}, \beta_k^\dagger, \beta_{-k})\begin{pmatrix}0&c_k&\sqrt{1-c_k^2}&0\\c_k&0&0&\sqrt{1-c_k^2}\\\sqrt{1-c_k^2}&0&0&-c_k\\0&\sqrt{1-c_k^2}&-c_k&0\end{pmatrix}\begin{pmatrix}\alpha_k\\\alpha^\dagger_{-k}\\\beta_k\\\beta^\dagger_{-k}\end{pmatrix}, \end{aligned} \tag{C2}$$

where $|c_k|\leqslant 1$. In the Heisenberg picture,

$$M^x(t)=\sum_k(\alpha_k^\dagger, \alpha_{-k}, \beta_k^\dagger, \beta_{-k})\begin{pmatrix}0&c_ke^{-2i\lambda_k t}&\sqrt{1-c_k^2}e^{it(l_k-\lambda_k)}&0\\c_ke^{2i\lambda_k t}&0&0&\sqrt{1-c_k^2}e^{-it(l_k-\lambda_k)}\\\sqrt{1-c_k^2}e^{-it(l_k-\lambda_k)}&0&0&-c_ke^{-2il_kt}\\0&\sqrt{1-c_k^2}e^{it(l_k-\lambda_k)}&-c_ke^{2il_kt}&0\end{pmatrix}\begin{pmatrix}\alpha_k\\\alpha^\dagger_{-k}\\\beta_k\\\beta^\dagger_{-k}\end{pmatrix}. \tag{C3}$$

We now calculate the linear and nonlinear magnetic susceptibilities of the TKSC. We first consider the linear susceptibility $\chi^{(1)}_{xx}(t)$. The starting point is the Kubo formula:

$$\begin{aligned} \chi^{(1)}_{xx}(t) &= \frac{i\Theta(t)}{L}\langle[M^x(t), M^x(0)]\rangle \\ &= \frac{i\Theta(t)}{L}\sum_{k>0}\left\langle\left[m^x_k(t), m^x_k(0)\right]\right\rangle \\ &= \frac{2}{L}\sum_{k>0}c_k^2(\sin(2l_kt)+\sin(2\lambda_kt)), \end{aligned} \tag{C4}$$

where $\langle\cdots\rangle$ represents the average in the ground state. The second equality comes from the fact that m^x_k with different k commute. The second order nonlinear susceptibility is given as

$$\begin{aligned} \chi^{(2)}_{xxx}(t,\tau+t) &= \frac{i^2\Theta(t)\Theta(\tau)}{L}\langle[[M^x(\tau+t), M^x(\tau)], M^x(0)]\rangle \\ &= \frac{i^2\Theta(t)\Theta(\tau)}{L}\sum_{k>0}\left\langle\left[\left[m^x_k(\tau+t), m^x_k(\tau)\right], m^x_k(0)\right]\right\rangle \\ &= 0. \end{aligned} \tag{C5}$$

As pointed out in the main text, the second order susceptibility of the TKSC vanishes. The formula for the third order nonlinear susceptibility is given as

$$\begin{aligned} \chi^{(3)}_{xxxx}(t_3, t_2+t_3, t_1+t_2+t_3) &= \frac{i^3\Theta(t_1)\Theta(t_2)\Theta(t_3)}{L}\langle[[[M^x(t_1+t_2+t_3), M^x(t_1+t_2)], M^x(t_1)], M^x(0)]\rangle \\ &= \frac{i^3\Theta(t_1)\Theta(t_2)\Theta(t_3)}{L}\sum_{k>0}\left\langle\left[\left[\left[m^x_k(t_1+t_2+t_3), m^x_k(t_1+t_2)\right], m^x_k(t_1)\right], m^x_k(0)\right]\right\rangle. \end{aligned} \tag{C6}$$

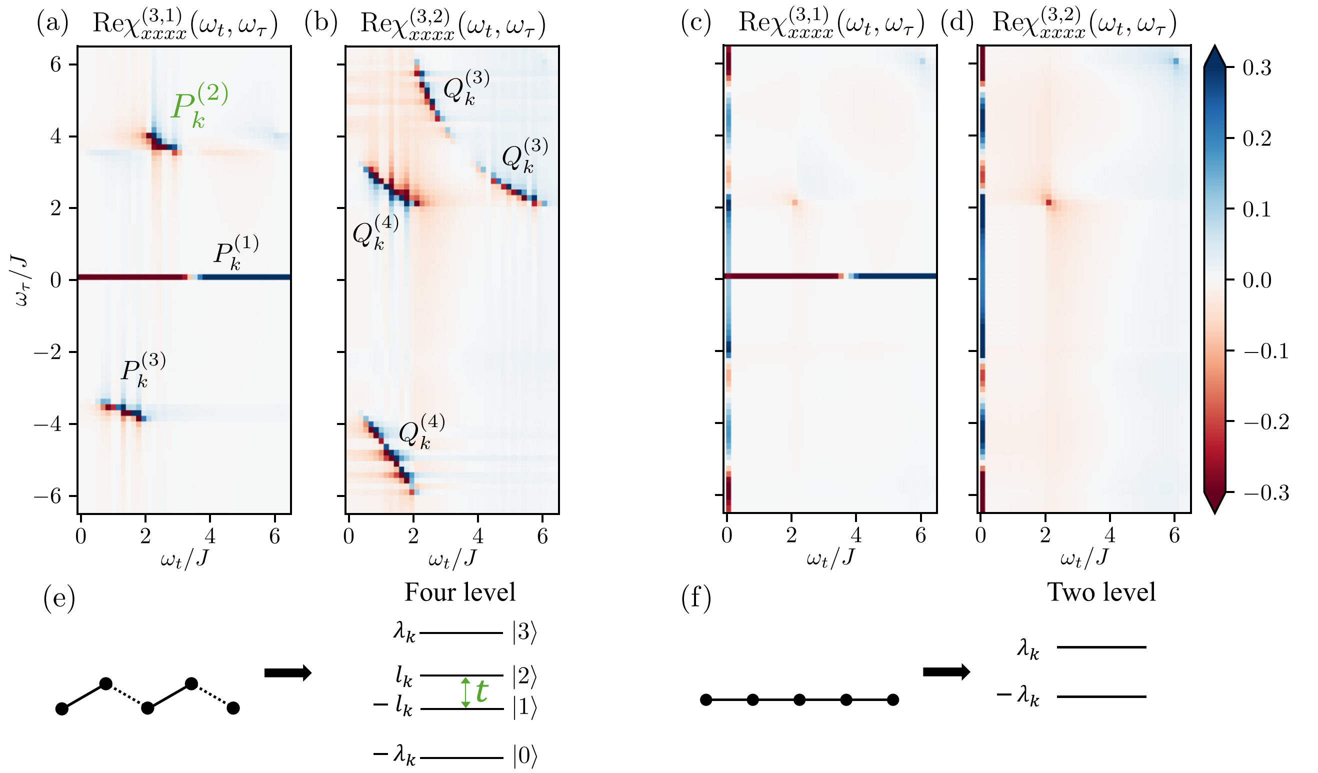

FIG. 5. (a), (b) Real part of Fourier transformed $\chi^{(3,1)}_{xxxx}(t,\tau+t,\tau+t)$ and $\chi^{(3,2)}_{xxxx}(t,t,\tau+t)$ of the TKSC (four level system). (c), (d) Real part of Fourier transformed $\chi^{(3,1)}_{xxxx}(t,\tau+t,\tau+t)$ and $\chi^{(3,2)}_{xxxx}(t,t,\tau+t)$ of the TFIC (two level system). Since $\mathrm{Re}\chi^{(2)}_{xxx}(\omega_t,\omega_\tau) = \mathrm{Re}\chi^{(2)}_{xxx}(-\omega_t,-\omega_\tau)$, the result is only shown in the first and fourth frequency quadrants.

We focus on the two limits which correspond to $\chi^{(3)}_{xxxx}$ measured in the two-pulse setup, $\chi^{(3,1)}_{xxxx}(t,\tau+t,\tau+t)$ with $t_1\to 0$, $t_2\to\tau$, $t_3\to t$, and $\chi^{(3,2)}_{xxxx}(t,t,t+\tau)$ with $t_1\to\tau$, $t_2\to 0$, $t_3\to t$:

$$\chi^{(3,1)}_{xxxx}(t,\tau+t,\tau+t) = \frac{\Theta(t)\Theta(\tau)}{L}\sum_{k>0} P_k^{(1)}+P_k^{(2)}+P_k^{(3)},$$

with

$$\begin{aligned}
P_k^{(1)} &= -8c_k^4[\sin(2l_k t)+(l_k\leftrightarrow\lambda_k)],\\
P_k^{(2)} &= 8\left(c_k^4-c_k^2\right)[\sin(2l_k t+(l_k+\lambda_k)\tau)+(l_k\leftrightarrow\lambda_k)],\\
P_k^{(3)} &= 8\left(c_k^2-c_k^4\right)[\sin((l_k-\lambda_k)t+(l_k+\lambda_k)\tau)+(l_k\leftrightarrow\lambda_k)],
\end{aligned}$$

and

$$\chi^{(3,2)}_{xxxx}(t,t,\tau+t) = \frac{\Theta(t)\Theta(\tau)}{L}\sum_{k>0} Q_k^{(1)}+Q_k^{(2)}+Q_k^{(3)}+Q_k^{(4)},$$

with

$$\begin{aligned}
Q_k^{(1)} &= -4c_k^2[\sin(2l_k(t+\tau))+(l_k\leftrightarrow\lambda_k)],\\
Q_k^{(2)} &= -4c_k^4[\sin(2l_k(t-\tau))+(l_k\leftrightarrow\lambda_k)],\\
Q_k^{(3)} &= 4\left(c_k^4-c_k^2\right)[\sin(2\lambda_k t+2l_k\tau)+(l_k\leftrightarrow\lambda_k)],\\
Q_k^{(4)} &= 8\left(c_k^2-c_k^4\right)[\sin((\lambda_k-l_k)t+2l_k\tau)+(l_k\leftrightarrow\lambda_k)],
\end{aligned}$$

where c_k is the matrix element of the magnetization as given in Eq. (C2).

In Fig. 5, we plot the real part of Fourier transformed $\chi^{(3,1)}_{xxxx}(t,\tau+t,\tau+t)$ and $\chi^{(3,2)}_{xxxx}(t,t,\tau+t)$ for the TKSC and TFIC. The formulation for the TFIC is explicitly given in Ref. [8]. $\chi^{(3)}_{xxxx}$ of the TKSC [Figs. 5(a) and 5(b)] contains the off-diagonal signals unlike $\chi^{(3)}_{xxxx}$ of the TFIC [Figs. 5(c) and 5(d)]. Such signals come from the transition between different excited states, whose presence originates from the bond dependent spin exchange interactions. For example, $P_k^{(2)}$ contains a transition between the first excited state $|1\rangle$ and the second excited state $|2\rangle$ as illustrated in Fig. 5(e), resulting in an oscillatory signal with frequency $2l_k$ throughout the time interval t.

APPENDIX D: SECOND ORDER SUSCEPTIBILITIES OF THE TKSC WITH TRANSVERSE FIELD

The TKSC with a transverse field along $\hat{x}$ direction is written as

$$H = -J\sum_{i=1}^{L'}(\tilde{\sigma}_{2i-1}(\theta)\tilde{\sigma}_{2i}(\theta)+\tilde{\sigma}_{2i}(-\theta)\tilde{\sigma}_{2i+1}(-\theta))-h_x\sum_{i=1}^{L}\sigma_i^x. \tag{D1}$$

We now rewrite the model in terms of spinless fermions using the Jordan-Wigner transformation:

$$H = \sum_{k>0}(a_k^\dagger, a_{-k}, b_k^\dagger, b_{-k})\hat{M}_k \begin{pmatrix} a_k \\ a_{-k}^\dagger \\ b_k \\ b_{-k}^\dagger \end{pmatrix}, \tag{D2}$$

where

$$\hat{M}_k = \begin{pmatrix} 2h_x & 0 & S_k & P_k + Q_k \\ 0 & -2h_x & P_k - Q_k & -S_k \\ S_k^* & P_k^* - Q_k^* & 2h_x & 0 \\ P_k^* + Q_k^* & -S_k^* & 0 & -2h_x \end{pmatrix},$$

with $P_k = iJ(1 + e^{ik})\sin 2\theta$, $Q_k = -J(1 - e^{ik})\cos 2\theta$, and $S_k = -J(1 + e^{ik})$. Using the Bogoliubov transformation,

$$(\gamma_k^\dagger, \gamma_{-k}, \eta_k^\dagger, \eta_{-k})\, \hat{U}_k = (a_k^\dagger, a_{-k}, b_k^\dagger, b_{-k}), \tag{D3}$$

Eq. (D2) can be diagonalized as

$$H = \sum_{k>0}\left[l_k(\gamma_k^\dagger\gamma_k - \gamma_{-k}\gamma_{-k}^\dagger) + \lambda_k(\eta_k^\dagger\eta_k - \eta_{-k}\eta_{-k}^\dagger)\right], \tag{D4}$$

where $l_k = \sqrt{\xi_k + 4h_x^2 - \sqrt{\xi_k^2 - \tau_k^2 + 16h_x^2|S_k|^2}}$ and $\lambda_k = \sqrt{\xi_k + 4h_x^2 + \sqrt{\xi_k^2 - \tau_k^2 + 16h_x^2|S_k|^2}}$, with $\xi_k = |P_k|^2 + |Q_k|^2 + |S_k|^2 + 4h_x^2$ and $\tau_k = |P_k^2 - Q_k^2 + S_k^2| + 4h_x^2$. Then, one can use the Kubo formula given in Appendix C to obtain nonlinear susceptibilities. In Fig. 6, we plot the real part of Fourier transformed $\chi_{xxx}^{(2)}(t, \tau + t)$ with a low $h_x/J = 1/20$ and strong $h_x/J = 1/2$ transverse field. As pointed out in the main text, the additional transverse field terms break the $\hat{z}$-glide symmetry of the TKSC and make $\chi_{xxx}^{(2)}$ finite with off-diagonal signals.

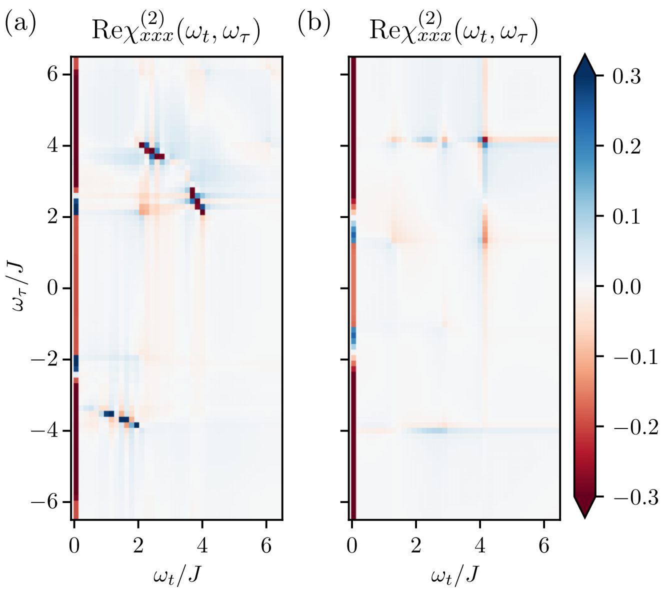

FIG. 6. Real part of Fourier transformed $\chi_{xxx}^{(2)}(t, \tau + t)$ of the TKSC with (a) a small transverse field $h_x/J = 1/20$ and (b) a strong transverse field $h_x/J = 1/2$.

[1] T. P. Devereaux and R. Hackl, Inelastic light scattering from correlated electrons, Rev. Mod. Phys. **79**, 175 (2007).

[2] P. Hamm and M. Zanni, *Concepts and Methods of 2D Infrared Spectroscopy* (Cambridge University Press, Cambridge, UK, 2011).

[3] K. E. Dorfman, F. Schlawin, and S. Mukamel, Nonlinear optical signals and spectroscopy with quantum light, Rev. Mod. Phys. **88**, 045008 (2016).

[4] S. Mukamel, Multidimensional femtosecond correlation spectroscopies of electronic and vibrational excitations, Annu. Rev. Phys. Chem. **51**, 691 (2000).

[5] T. Zhang, I. Kuznetsova, T. Meier, X. Li, R. P. Mirin, P. Thomas, and S. T. Cundiff, Polarization-dependent optical 2d fourier transform spectroscopy of semiconductors, Proc. Natl. Acad. Sci. USA **104**, 14227 (2007).

[6] S. T. Cundiff and S. Mukamel, Optical multidimensional coherent spectroscopy, Phys. Today **66**, 44 (2013).

[7] J. Lu, X. Li, H. Y. Hwang, B. K. Ofori-Okai, T. Kurihara, T. Suemoto, and K. A. Nelson, Coherent two-dimensional terahertz magnetic resonance spectroscopy of collective spin waves, Phys. Rev. Lett. **118**, 207204 (2017).

[8] Y. Wan and N. P. Armitage, Resolving continua of fractional excitations by spinon echo in THz 2D coherent spectroscopy, Phys. Rev. Lett. **122**, 257401 (2019).

[9] Z.-L. Li, M. Oshikawa, and Y. Wan, Photon echo from lensing of fractional excitations in Tomonaga-Luttinger spin liquid, Phys. Rev. X **11**, 031035 (2021).

[10] W. Choi, K. H. Lee, and Y. B. Kim, Theory of two-dimensional nonlinear spectroscopy for the Kitaev spin liquid, Phys. Rev. Lett. **124**, 117205 (2020).

[11] R. M. Nandkishore, W. Choi, and Y. B. Kim, Spectroscopic fingerprints of gapped quantum spin liquids, both conventional and fractonic, Phys. Rev. Res. **3**, 013254 (2021).

[12] Y. Qiang, V. L. Quito, T. V. Trevisan, and P. P. Orth, Probing majorana wave functions in Kitaev honeycomb spin liquids with second-order two-dimensional spectroscopy, arXiv:2301.11243.

[13] O. Hart and R. Nandkishore, Extracting spinon self-energies from two-dimensional coherent spectroscopy, Phys. Rev. B **107**, 205143 (2023).

[14] M. Fava, S. Gopalakrishnan, R. Vasseur, F. H. Essler, and S. Parameswaran, Divergent nonlinear response from quasiparticle interactions, arXiv:2208.09490.

[15] Q. Gao, Y. Liu, H. Liao, and Y. Wan, Two-dimensional coherent spectrum of interacting spinons from matrix product states, Phys. Rev. B **107**, 165121 (2023).

[16] M. Fava, R. Coldea, and S. Parameswaran, Glide symmetry breaking and Ising criticality in the quasi-1d magnet $CoNb_2O_6$, Proc. Natl. Acad. Sci. USA **117**, 25219 (2020).

[17] C. Morris, N. Desai, J. Viirok, D. Hüvonen, U. Nagel, T. Room, J. Krizan, R. Cava, T. McQueen, S. Koohpayeh *et al.*, Duality and domain wall dynamics in a twisted kitaev chain, Nat. Phys. **17**, 832 (2021).

[18] I. Maartense, I. Yaeger, and B. Wanklyn, Field-induced magnetic transitions of $CoNb_2O_6$ in the ordered state, Solid State Commun. **21**, 93 (1977).

[19] S. Kobayashi, S. Mitsuda, M. Ishikawa, K. Miyatani, and K. Kohn, Three-dimensional magnetic ordering in the quasi-one-dimensional Ising magnet $CoNb_2O_6$ with partially released geometrical frustration, Phys. Rev. B **60**, 3331 (1999).

[20] R. Coldea, D. Tennant, E. Wheeler, E. Wawrzynska, D. Prabhakaran, M. Telling, K. Habicht, P. Smeibidl, and K. Kiefer, Quantum criticality in an Ising chain: experimental evidence for emergent E_8 symmetry, Science **327**, 177 (2010).

[21] C. M. Morris, R. Valdes Aguilar, A. Ghosh, S. M. Koohpayeh, J. Krizan, R. J. Cava, O. Tchernyshyov, T. M. McQueen, and N. P. Armitage, Hierarchy of bound states in the one-dimensional ferromagnetic Ising chain $CoNb_2O_6$ investigated by high-resolution time-domain terahertz spectroscopy, Phys. Rev. Lett. **112**, 137403 (2014).

[22] A. W. Kinross, M. Fu, T. J. Munsie, H. A. Dabkowska, G. M. Luke, S. Sachdev, and T. Imai, Evolution of quantum fluctuations near the quantum critical point of the transverse field Ising chain system $CoNb_2O_6$, Phys. Rev. X **4**, 031008 (2014).

[23] K. Amelin, J. Engelmayer, J. Viirok, U. Nagel, T. Rõõm, T. Lorenz, and Z. Wang, Experimental observation of quantum many-body excitations of E_8 symmetry in the Ising chain ferromagnet $CoNb_2O_6$, Phys. Rev. B **102**, 104431 (2020).

[24] K. Amelin, J. Viirok, U. Nagel, T. Rõõm, J. Engelmayer, T. Dey, A. A. Nugroho, T. Lorenz, and Z. Wang, Quantum spin dynamics of quasi-one-dimensional heisenberg-Ising magnets in a transverse field: confined spinons, E_8 spectrum, and quantum phase transitions, J. Phys. A: Math. Theor. **55**, 484005 (2022).

[25] Y. Xu, L. S. Wang, Y. Y. Huang, J. M. Ni, C. C. Zhao, Y. F. Dai, B. Y. Pan, X. C. Hong, P. Chauhan, S. M. Koohpayeh, N. P. Armitage, and S. Y. Li, Quantum critical magnetic excitations in spin-1/2 and spin-1 chain systems, Phys. Rev. X **12**, 021020 (2022).

[26] S. Kobayashi, S. Mitsuda, and K. Prokes, Low-temperature magnetic phase transitions of the geometrically frustrated isosceles triangular Ising antiferromagnet $CoNb_2O_6$, Phys. Rev. B **63**, 024415 (2000).

[27] S. R. White, Density matrix formulation for quantum renormalization groups, Phys. Rev. Lett. **69**, 2863 (1992).

[28] G. Vidal, Classical simulation of infinite-size quantum lattice systems in one spatial dimension, Phys. Rev. Lett. **98**, 070201 (2007).

[29] G. B. Sim, J. Knolle, and F. Pollmann, Nonlinear spectroscopy of bound states in perturbed Ising spin chains, Phys. Rev. B **107**, L100404 (2023).

[30] J. A. Kjäll, F. Pollmann, and J. E. Moore, Bound states and E_8 symmetry effects in perturbed quantum Ising chains, Phys. Rev. B **83**, 020407(R) (2011).

[31] N. J. Robinson, F. H. L. Essler, I. Cabrera, and R. Coldea, Quasiparticle breakdown in the quasi-one-dimensional Ising ferromagnet $CoNb_2O_6$, Phys. Rev. B **90**, 174406 (2014).

[32] W.-L. You, Y.-C. Qiu, and A. M. Oleś, Quantum phase transitions in a generalized compass chain with three-site interactions, Phys. Rev. B **93**, 214417 (2016).

[33] J. Yang, W. Yuan, T. Imai, Q. Si, J. Wu, and M. Kormos, Local dynamics and thermal activation in the transverse-field Ising chain, Phys. Rev. B **106**, 125149 (2022).

[34] P. Laurell, G. Alvarez, and E. Dagotto, Spin dynamics of the generalized quantum spin compass chain, Phys. Rev. B **107**, 104414 (2023).

[35] S. Paeckel, T. Köhler, A. Swoboda, S. R. Manmana, U. Schollwöck, and C. Hubig, Time-evolution methods for matrix-product states, Ann. Phys. (NY) **411**, 167998 (2019).

[36] L. Woodland, I. Lovas, M. Telling, D. Prabhakaran, L. Balents, and R. Coldea, Excitations of quantum Ising chain $CoNb_2O_6$ in low transverse field: quantitative description of bound states stabilized by off-diagonal exchange and applied field, arXiv:2306.01948.

[37] G. Vidal, Efficient classical simulation of slightly entangled quantum computations, Phys. Rev. Lett. **91**, 147902 (2003).

[38] S. R. White and A. E. Feiguin, Real-time evolution using the density matrix renormalization group, Phys. Rev. Lett. **93**, 076401 (2004).

[39] G. Sim, F. Pollmann, and J. Knolle, Shedding light on microscopic details: 2D spectroscopy of 1d quantum Ising magnets, https://doi.org/10.5281/zenodo.7886700 (2023).

[40] J. Hauschild and F. Pollmann, Efficient numerical simulations with tensor networks: tensor network python (tenpy), SciPost Phys. Lecture Notes **2018**, 5 (2018).

[41] G. Vidal, Efficient simulation of one-dimensional quantum many-body systems, Phys. Rev. Lett. **93**, 040502 (2004).

[42] S. R. White and I. Affleck, Spectral function for the $s = 1$ Heisenberg antiferromagetic chain, Phys. Rev. B **77**, 134437 (2008).

[43] R. Verresen, R. Moessner, and F. Pollmann, Avoided quasiparticle decay from strong quantum interactions, Nat. Phys. **15**, 750 (2019).